Silicon Photomultipliers:
Characterization and Applications

Marco Ramilli[1], Alessia Allevi[1], Luca Nardo[1],
Maria Bondani[2] and Massimo Caccia[1]
[1]*Dipartimento di Fisica e Matematica - Università degli Studi dell'Insubria*
[2]*Istituto di Fotonica e Nanotecnologie - Consiglio Nazionale delle Ricerche*
Italy

1. Introduction

Silicon Photo-Multipliers (SiPMs henceover) are photo-detectors based on a technology originally invented in Russia (Akindinov et al., 1997). They essentially consist of an *array of p-n junctions* operated beyond the breakdown voltage (McKay, 1954), in a Geiger-Müller (G-M) regime (Oldham et al., 1972), with typical gain of the order of 10^6 and on-cell integrated quenching mechanisms. Silicon photo-detectors with internal multiplication are in use since more than a decade (Lutz, 1995). Avalance Photo-Diodes (APDs) (Akindinov et al., 2005) are operated in a proportional regime, with typical gains of 10^4, Single-Photon Avalanche Diodes (SPADs) (Cova et al., 1996) are endowed with single-photon sensitivity and are tailored for high frequency counting with time resolutions down to 30 ps. However, being made of a single cell operated in binary mode, they do not carry any information about the intensity of the incoming light field.

SiPMs complement the family of existing sensors: with a cell density of $\sim 10^3/\mathrm{mm}^2$, areas up to 3×3 mm^2 and *a single output node*, they offer the possibility of measuring the intensity of the light field simply by counting the number of fired cells. The main features of SiPMs, due to their structural and operational characteristics are:

- high gain, granted by G-M operating mode, comparable to the values achieved by standard photomultipliers (PMTs);
- enhanced linearity, owing to cell structure, with deviations that become relevant when the average number of detected photons approaches the same order of magnitude of the number of cells of the device (Tarolli et al., 2010);
- large dynamic range, provided by the pixelated structure with a common output, spanning from the single photon regime up to high intensities;
- operability in magnetic fields, compactness and relatively low cost, granted by silicon-based technology.

On the other hand, since G-M avalanches that are triggered by electron-hole pairs extracted by the impinging photons are obviously indistinguishable from the ones originated from other processes, dealing with all possible sources of noise is far from being trivial:

- thermally extracted electron-hole pairs cause high Dark Count Rates (DCR), with values ranging from several hundreds of kHz up to the MHz level, depending on the total number of cells, the operating temperature and the overbias;

- spurious signals are also due to optical cross-talk (Sciacca et al., 2008): photons emitted by an avalanche can travel through silicon and reach the depleted region in a neighboring cell, thus triggering another avalanche;

- carriers extracted during an avalanche process may be trapped in a false potential minimum in the depleted region: escaping from that trap they can originate an *afterpulse* avalanche, so called because it typically happens shortly after (or even during) the recovery of the previous avalanche (Du et al., 2008; Eckert et al., 2010).

These apparently huge disadvantages can be overridden by means of an exhaustive characterization of the SiPM performances. An example of this procedure will be given in the following Section, where we present the characterization of the devices as a function of temperature.

Another aspect of the characterization of SiPMs will be addressed by providing a description of the G-M avalanches probability distribution functions, in order to reconstruct the statistics of the impinging light (Ramilli et al., 2010).

Modeling the SiPM response is also preliminary to application of these sensors as detectors in Fluorescence Fluctuation Spectroscopy biophysical experiments (Chen et al., 1999; Schwille, 2001), where the parameters describing the system under investigation are inferred by the deviations of the fluorescence intensity of suitable probes around its mean value. A feasibility study on this topic will be presented in the final part of the Chapter.

2. Characterization

Tests have been performed on existing devices with the main goal to define an exhaustive characterization protocol and to produce a comparative study. Three kinds of detectors from different manufacturers have been studied: SensL[1], Hamamatsu Photonics[2] and STMicroelectronics[3]. Detector characterization is a major task for all the applications of SiPMs and in particular for the identification of critical parameters: for example, DCR is an important parameter for low-rate-event applications, while thermal stability is essential for portable devices. For this reason, the following characterization protocol has been developed assessing:

- Geometrical parameters (number of cells, size of detectors and occupancy factor);
- I–V measurements;
- Noise measurements: DCR, optical cross-talk, dependence on the environmental parameters.
- Analysis of photon spectra: resolution power, gain, working point optimization (at low and large flux), electronic noise measurement taking into account cell-to-cell variations, dependence on the environmental parameters (temperature).
- Linearity and dynamic range.
- Spectral response measurement: photon detection efficiency (PDE).

---

[1] see http://sensl.com/.
[2] see http://www.hamamatsu.com/.
[3] see http://www.st.com/stonline/.

In particular, studies of the main SiPM parameters (such as gain, PDE, DCR and optical cross-talk) as functions of temperature will be described in details.

2.1 Experimental setup

In order to implement the characterization protocol, we have developed an experimental setup in which a green-emitting LED (λ = 510 nm), coupled to a fast pulse generator (PDL800-B PicoQuant), has been used as the light source. The SiPM output signal has been elaborated in the following way:

- SiPM was directly connected to a first stage amplification board:
  - in experimental situations where the SiPM was operated under a continuous light flux, a transimpedance pre-amplifier provided by SensL has been used: this device converts the raw current from the SiPM into a voltage, with an amplification of 470 V/A;
  - when the SiPM was operated in the pulsed regime, a different pre-amplifier, called Pulse Amplifier and also provided by SensL, has been used. It allowed the fast rise of the detector to be exploited, providing an amplification factor of 20;
- a leading edge discriminator (Lecroy 821) with a user-defined voltage threshold that the SiPM output has to exceed in order to provide a triggering signal has been then exploited at the output of the amplifier;
- in case of frequency measurements (e.g. DCR measurements), the discriminator output has been directly sent to a scaler;
- the output of the SiPM has been integrated by a CAEN QDC V792N board:
  - the board provides a charge measurement performing the integration of the input voltage signal, with a conversion time of 2.8 μs and a reset time of 4 μs;
  - the integration gate is generated by a NIM timing unit and must precede the analog input signal of at least 15 ns;
- data have been stored in a PC via a USB-VME Bridge (CAEN).

The system composed by the investigated SiPM and the first-stage amplification board has been located in a metal box sealed with grease, in which air has been replaced with helium. The cooling fluid has been pumped into the box through a copper pipe, allowing controlled temperature variations. The temperature of the system has been measured by a thermistor placed in contact with the external packaging of the sensor.

2.2 Studying temperature behavior

In order to quantitatively understand the effects of temperature changes on the SiPM main figures of merit, a suitable set of measurements must be accomplished. The procedure has been tested with SensL CSI 0747 015 A20 HD and the results regarding this sensor will be presented in more detail in the following. Once the procedure was tested, it has been repeated with different SiPM models: a SensL CSI 0740 001 A20 HD, a Hamamatsu S10362-11-100C and a ST Microelectronics TO-8 prototype.

Sensors have been placed in the cooling box described in Section 2.1 and several spectra have been acquired at different bias voltages and different temperatures in order to obtain the values of gain and PDE. Moreover, DCR measurements at different thresholds were used to evaluate both DCR and cross-talk contributions. To analyze the procedure in detail, a typical
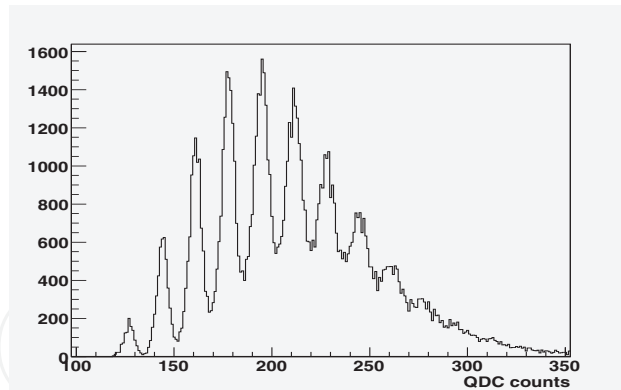
Fig. 1. Example of a low flux spectrum of a SiPM; each histogram bin represents a single QDC channel corresponding to 0.11 pC.

low-flux spectrum is presented in Fig. 1 that shows the charge measurements performed by the CAEN QDC: a waveform generator triggered both the light source and the *gate* needed to perform the charge measurement. The structure of the histogram reflects the characteristics of the SiPM, since the n-th peak position represents the most probable output value (in released charge) of n cells firing simultaneously and its Gaussian broadening is due to stochastic noise sources. In this experimental situation, the very first peak represents the *zero-photon* peak, i.e. the output of the QDC board with no SiPM signal. The broadening of the n-th peak σ_n can be described with good approximation as:

$$\sigma_n^2 = \sigma_0^2 + n\sigma_1^2, \tag{1}$$

where σ_0 is the variance of the zero-photon peak (giving the noise contribution due to the electronic chain), and σ_1 is the variance of the first photon peak, providing an estimation of the SiPM noise.

2.2.1 Gain

The gain has been evaluated by illuminating the SiPM with a low photon flux, thus obtaining a spectrum whose peaks are clearly recognizable (see Fig. 1). As the n-th peak corresponds to the mean charge released by n G-M avalanches, the gain G can be computed in the following way:

$$G = \frac{QDC_{cal}}{e^- K_{amp}} \Delta_{PP}, \tag{2}$$

where $QDC_{cal} = 0.11$ pC/channel is the charge corresponding to one QDC unit, e^- is the elementary charge, K_{amp} is the global amplification factor of the electronic setup, and Δ_{PP} is the distance in QDC units between two adjacent peaks of the collected spectra.

The gain behavior as a function of the bias voltage, at fixed temperatures, is shown in Fig. 2: a linear dependence in the range of interest is clearly observable with a slope independent of the temperature within the experimental errors. In Fig. 3 the same gain values are presented as functions of temperature, for fixed bias voltages: a linear behavior is still clearly recognizable; in this case as well the slope is not affected by the change of the applied bias.

This analysis suggests that the gain can be expressed as a linear function of a variable which can be re-scaled with temperature. Since it is well known that the breakdown voltage has, in

SiPM Model	m_{BD} (mV/degree)
SensL CSI 0747 015 A20 HD	23.2 ± 1.4
SensL CSI 0740 001 A20 HD	23.6 ± 0.9
Hamamatsu S10362-11-100C	61.9 ± 0.7
STM TO-8 prototype	31.5 ± 0.1

Table 1. Rate of change of the breakdown voltage with temperature.

our range of interest, a linear dependence on temperature (Goetzberger et al., 1963), the over voltage, defined as the difference between the applied bias voltage and the breakdown one, is thus a suitable candidate. The conditions can be summarized as follows

$$G(V, T) = m_V(V - V_{BD}(T)), \tag{3}$$

$$G(V, T) = m_T T + G(T_0, V), \tag{4}$$

where m_V and m_T are the slopes, $V_{BD}(T)$ is the breakdown voltage and T_0 is a reference temperature. Solving these equations for $V_{BD}(T)$, the rate of change of the breakdown voltage with temperature can be expressed as:

$$m_{BD} = -\frac{m_T}{m_V}. \tag{5}$$

The procedure has been applied to the different SiPMs. From the results in Table 1, we can see that the values of m_{BD} are technology dependent.

By using the breakdown voltage value measured at room temperature (RT) as the reference
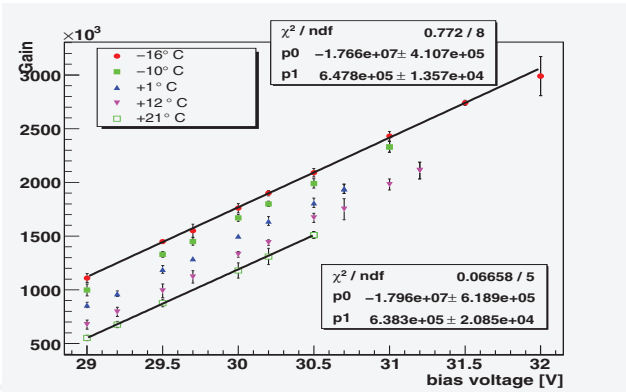

Fig. 2. Gain as a function of bias voltage, for different temperatures; a linear fit has been performed for each temperature set: the obtained fit slopes are in agreement.

value, the breakdown values for each temperature can be written as:

$$V_{BD}(T) = m_{BD}(T - T_{RT}) + V_{BD}(T_{RT}). \tag{6}$$

From Equation 6 it is possible to express the gain and all the other measured parameters as a function of the over voltage: in Fig. 4 the gain is plotted as a function of the over voltage, showing a global linear behavior independent of the temperature. Equation 6 can be used to fix the operational parameters of a SiPM regardless of the varying environmental conditions: if m_{BD} is known with enough precision and frequent measurements of the SiPM temperature are performed, the over voltage across each cell can be maintained fixed by simply continuously adjusting the applied bias according to the temperature variations. This
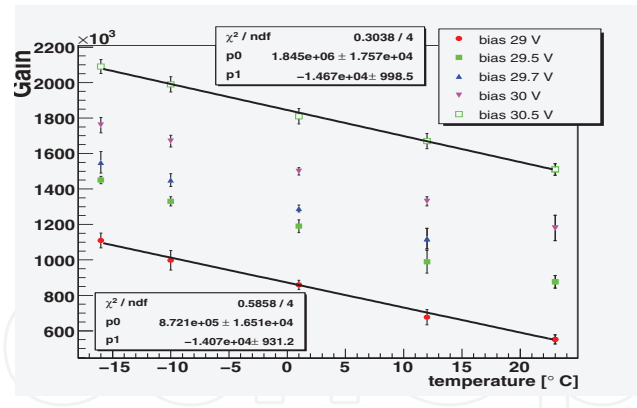
Fig. 3. Gain as a function of temperature (expressed in Celsius degrees), for fixed bias voltages; each set has been fitted using a linear law: the obtained slopes are in agreement.
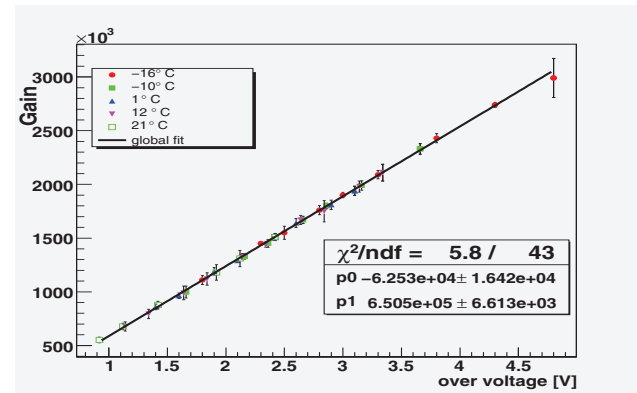

Fig. 4. Gain as a function of the over voltage: values are obtained by calculating the breakdown voltage for each temperature; all the data acquired at different temperatures have been fitted with the same linear law.

idea has led to a collaboration between Università dell'Insubria and CAEN for the realization of CAEN SP5600 General Purpose Power Supply and Amplification Unit module with an integrated threshold discriminator.

2.2.2 Dark count rate

As explained in Section 1, DCR is the frequency of the G-M avalanches triggered by thermally extracted carriers. A scan of the DCR at different thresholds can be done, and the resulting plot (an example is shown in Fig. 5) is usually referred to as *staircase function*.
DCR has been measured at different voltages and different temperatures, also setting different discrimination thresholds; in Fig. 6, for example, the results for a *"half photon threshold"* are shown. A clear and expected dependence on temperature is recognizable.
An exhaustive knowledge of DCR behavior is of utmost importance for a complete characterization of all the noise sources of the detector. It can be a fundamental figure of merit for low flux applications.

2.2.3 Optical cross-talk

An electron avalanche is modeled as a microplasma (Oldham et al., 1972): photons emitted by the accelerated carriers during this event have a certain probability to reach the neighboring
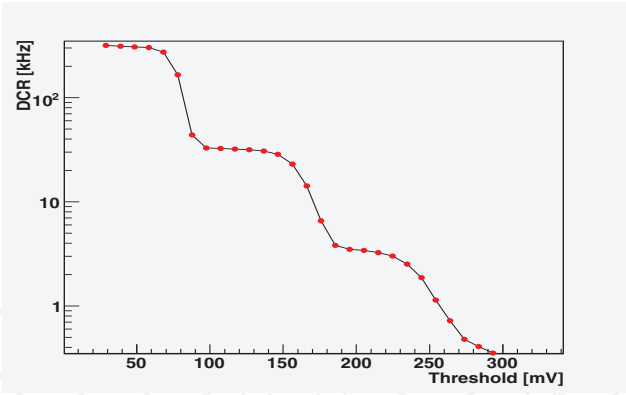
Fig. 5. Example of *staircase curve*, obtained after a three-stage amplification.
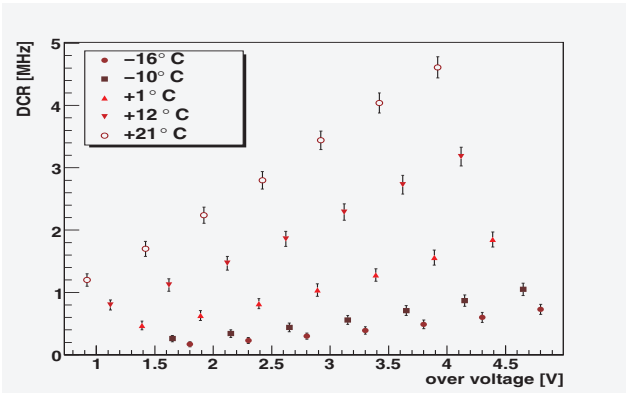

Fig. 6. DCR at different temperatures as a function of the over voltage, for a SensL SiPM.
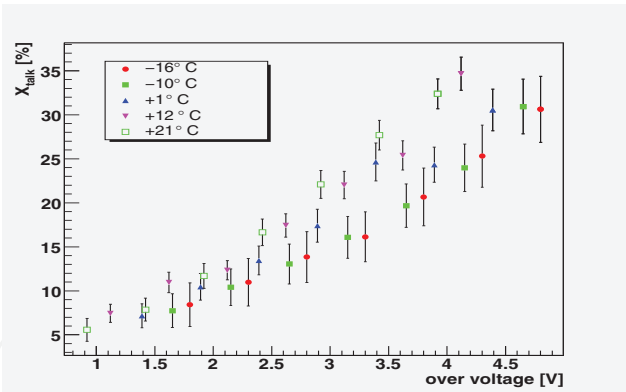

Fig. 7. Cross-talk as a function of the over voltage, at different temperatures, for a SensL SiPM.

cell diodes thus triggering a second avalanche. The quantity named optical cross-talk (in short cross-talk, X_T) is simply the percentage of avalanches triggered by such a mechanism.

Cross-talk has been calculated starting from DCR measurements by taking the ratio between the DCR frequencies with the discriminator threshold respectively at *"one-and-half photon"* and at *"half photon"*. This method is based on the assumption that the probability that two uncorrelated thermally-triggered avalanches are generated within the same rise time is negligible, so that all the second photon events are due to cross-talk.

In Fig. 7 the results of the cross-talk evaluation are presented: it is worth noting that, within the experimental errors, cross-talk does not seem to suffer a strong temperature dependence.

2.2.4 Photon detection efficiency

Photon detection efficiency (PDE) is a key parameter for every light detector and is defined as the product of three terms:
- quantum efficiency, that is the probability that the impinging photon produces a charge carrier, which is a function of the incoming light wavelength;
- the G-M probability that the extracted carrier generates an avalanche that depends on the over voltage;
- the so-called Fill Factor (FF), a geometrical factor that expresses the portion of the active area of the sensor with respect to the total area.
The PDE value thus represents the fraction of impinging photons that are actually detected.

To measure this quantity, SiPMs have been illuminated with a light intensity Φ which has been previously measured with a calibrated PMT HAMAMATSU H5783 and the resulting spectra have been acquired. PDE has been evaluated by estimating the mean number of detected photons $< n >_{meas}$ with respect to the incoming light intensity:

$$PDE = \frac{< n >_{meas}}{\Phi} \tag{7}$$

In the case of spectra in which each photon peak could be resolved, $< n >_{meas}$ has been obtained by fitting the peak positions with a Poissonian curve and by evaluating the mean value of the fit distribution. In the case in which the peaks could not be resolved, $< n >_{meas}$ has been estimated as

$$< n >_{meas} = \frac{QDC_{cal}}{e^- \, G \, K_{amp}} \Delta QDC \tag{8}$$

where G is the proper gain value, e^- is the elementary charge, $QDC_{cal} = 0.11$ pC is the charge per QDC unit, K_{amp} is the amplification factor of the electronics chain, and ΔQDC is the difference between the mean value of the obtained spectrum and the pedestal position.

However, this method provides a zero-order approximation of the PDE because it does not take into account cross-talk effects that can be as large as 40% (see Fig. 7 as a reference). To properly estimate the "*true*" number $< n >_0$ of impinging photons triggering an avalanche, the following relation has been used:

$$< n >_{meas} = \frac{< n >_o}{1 - X_T} \simeq < n >_o (1 + X_T). \tag{9}$$

The approximation is valid for small values of the cross-talk; the previously obtained PDE values have thus been corrected using $< n >_0$ as the mean number of detected photons as shown in Fig. 8. Again, PDE does not seem to have any remarkable temperature dependance, thus confirming the agreement of our results with the definition of PDE.

3. Photon-number statistics

Due to their good linear response, SiPMs can be considered as the ideal candidates for the reconstruction of the statistics of any light state (Afek et al., 2009). Obviously, the presence of DCR and cross-talk effects must be taken into account. A proper model of the detector
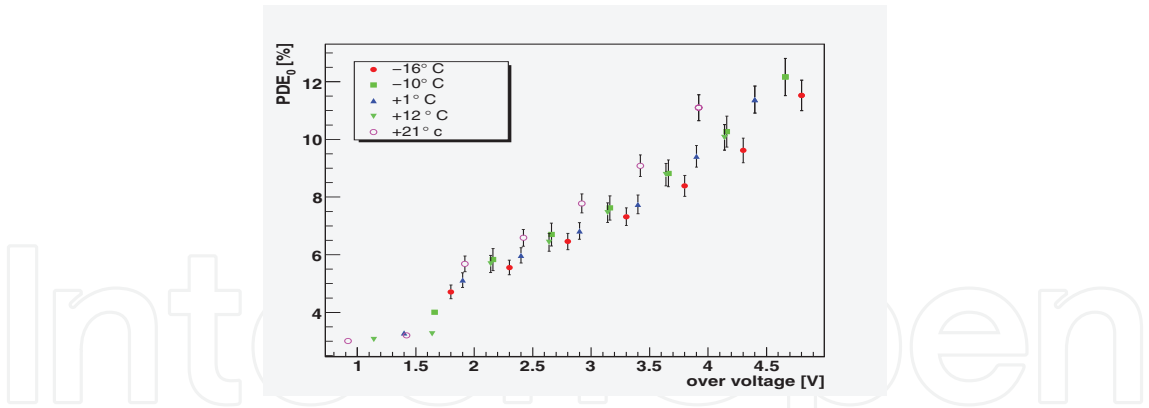
Fig. 8. PDE values corrected taking into account cross-talk effects, for a SensL SiPM. The wavelength of the impinging light is 510 nm.

	Hamamatsu MPPC S10362-11-100C
Number of Diodes:	100
Area:	1 mm × 1 mm
Diode dimension:	100 μm × 100 μm
Breakdown Voltage:	69.23 V
Dark Count Rate:	540 kHz at 70 V
Optical Cross-Talk:	25 % at 70 V
Gain:	3.3 · 10^6 at 70 V
PDE (green):	15 % at 70 V

Table 2. Main features of the SiPM MPPC S10362-11-100C (Hamamatsu). The data refer to room temperature.

response is thus required in order to properly assess the statistical properties of the light field under investigation (Ramilli et al., 2010). In the following Section we present two different analysis methods, both validated by suitable measurements performed by using a SiPM produced by Hamamatsu Photonics. In particular, to keep DCR and cross-talk effects at reasonable levels and to optimize the PDE, a detector endowed with 100 cells was chosen (MPPC S10362-11-100C, see Table 2). To test the model, the sensor was illuminated by the pseudo-thermal light obtained by passing the second-harmonics (@ 523 nm, 5.4-ps pulse duration) of a mode-locked Nd:YLF laser amplified at 500 Hz (High Q Laser Production) through a rotating ground-glass diffuser (D in Fig.8). The light to be measured was delivered to the sensor by a multimode optical fiber (1 mm core diameter). The detector response was integrated by the charge digitizer V792 by Caen. The signal was typically integrated over a 200-ns-long time window synchronized with the laser pulse.

3.1 Detector response modeling

The response of an ideal detector to a light field can be described as a Bernoullian process (Mandel & Wolf, 1995):

$$B_{m,n}(\eta) = \binom{n}{m} \eta^m (1-\eta)^{n-m} \tag{10}$$

being n the number of impinging photons over the integration time, m the number of detected photons and $\eta < 1$ the PDE. Actually, η is a single parameter quantifying detector effects and

losses (intentional or accidental) due to the optical system. As a consequence, the distribution $P_{m,\text{det}}$ of the number of detected photons has to be linked to the distribution $P_{n,\text{ph}}$ of the number of photons in the light under measurement by (Agliati et al., 2005; Mandel & Wolf, 1995; Zambra et al., 2004):

$$P_{m,\text{det}} = \sum_{n=m}^{\infty} B_{m,n}(\eta) P_{n,\text{ph}} \tag{11}$$

It can be demonstrated (Bondani et al., 2009a) that for a combination of classical light states the statistics is preserved by the primary detection process. This simple description has to be further developed to link $P_{m,\text{det}}$ to the probability density distribution of the G-M avalanches of any origin. First we must take into account spurious hits and cross-talk effects, not negligible in the detectors under study. The DCR results in a Poissonian process that can be described as:

$$P_{m,\text{dc}} = \overline{m}_{\text{dc}}^m / m! \exp(-\overline{m}_{\text{dc}}) \tag{12}$$

where $\overline{m}_{\text{dc}}$ is the mean number of dark counts during the gate window and $\sigma_{m,\text{dc}}^{(2)} = \sigma_{m,\text{dc}}^{(3)} = \overline{m}_{\text{dc}}$. As a consequence, the statistics of the recorded pulses may be described as:

$$P_{m,\text{det+dc}} = \sum_{i=0}^{m} P_{i,\text{dc}} P_{m-i,\text{det}} \tag{13}$$

obviously shifting the mean value and increasing variance and third-order central moment in the following way: $\overline{m}_{\text{det+dc}} = \overline{m}_{\text{det}} + \overline{m}_{\text{dc}}$, $\sigma_{m,\text{det+dc}}^{(2)} = \sigma_{m,\text{det}}^{(2)} + \overline{m}_{\text{dc}}$ and $\sigma_{m,\text{det+dc}}^{(3)} = \sigma_{m,\text{det}}^{(3)} + \overline{m}_{\text{dc}}$. As a further step, cross-talk effects must be taken into account. Cross-talk is a genuine cascade phenomenon that can be described at first order as (Afek et al., 2009)

$$C_{k,l}(x_t) = \binom{l}{k-l} x_t^{k-l} (1-x_t)^{2l-k}. \tag{14}$$

being x_t the (constant) probability that the G-M avalanche of a cell triggers a second cell (which becomes equivalent to the cross-talk probability X_T in the limit of $X_T \to 0$), l the number of dark counts and photo-triggered avalanches and k the actual light signal amplitude. Within this first-order approximation, the real sensor response is described by

$$P_{k,\text{cross}} = \sum_{m=0}^{k} C_{k,m}(x_t) P_{m,\text{det+dc}} \tag{15}$$

characterized by $\overline{k}_{\text{cross}} = (1+x_t)\overline{m}_{\text{det+dc}}$, $\sigma_{k,\text{cross}}^{(2)} = (1+x_t)^2 \sigma_{m,\text{det+dc}}^{(2)} + x_t(1-x_t)\overline{m}_{m,\text{det+dc}}$ and $\sigma_{k,\text{cross}}^{(3)} = (1+x_t)^3 \sigma_{m,\text{det+dc}}^{(3)} + 3x_t(1-x_t^2)\sigma_{m,\text{det+dc}}^{(2)} + x_t(1-3x_t+2x_t^2)\overline{m}_{m,\text{det+dc}}$.

In the following we refer to this analytical model as *Method I* and compare it with a better refined model (*Method II*). This second method offers, in principle, an extended range of application even if it is limited to a numerical rather than an analytical solution. Irrespective of the model, the amplification and digitization processes that produce the output x can be simply described as a multiplicative parameter G:

$$P_{x,\text{out}} = G P_{Gk,\text{cross}} \tag{16}$$

whose moments are $\overline{x}_{\text{out}} = G\overline{k}_{\text{cross}}$, $\sigma_{x,\text{out}}^{(2)} = G^2 \sigma_{k,\text{cross}}^{(2)}$ and $\sigma_{x,\text{out}}^{(3)} = G^3 \sigma_{k,\text{cross}}^{(3)}$.

3.1.1 Method I: an analytical evaluation of the second and third order momenta

In Ref. (Bondani et al., 2009b) we presented a self-consistent method aimed at reconstructing the statistics of detected photons. According to this method, the analysis of the output of the detector is based on the assumptions that the detection process is described by a Bernoullian convolution and that the overall amplification-conversion process is given by a very precise constant factor G, which allows the shot-by-shot detector output to be converted into the number of detected photons. Experimentally, the value of G can be obtained by detecting a light field at different optical losses and keeping the detector parameters fixed. Once the amplification-conversion factor has been evaluated, the detected-photon distribution can be achieved by dividing the output values by G and re-binning the data in unitary bins. Here we present the extension of the method to detectors with a significant DCR and first order cross-talk effects. The second-order momentum of the recorded pulse distribution $P_{x,\text{out}}$ can be used to evaluate the Fano factor:

$$F_{x,\text{out}} = \frac{\sigma^{(2)}_{x,\text{out}}}{\overline{x}_{\text{out}}} = \frac{Q_{\text{det+dc}}}{\overline{m}_{\text{det+dc}}}\overline{x}_{\text{out}} + G\frac{1+3x_t}{1+x_t} \, , \tag{17}$$

where $Q_{\text{det+dc}} = \sigma^{(2)}_{m,\text{det+dc}}/\overline{m}_{\text{det+dc}} - 1$ is the Mandel factor of the primary charges. Note that, due to dark counts, the coefficient of $\overline{x}_{\text{out}}$ in Equation 17 cannot be written as $Q_{\text{ph}}/\overline{n}$ (Andreoni & Bondani, 2009; Bondani et al., 2009b), that is, the coefficient $Q_{\text{det+dc}}/\overline{m}_{\text{det+dc}}$ does not only depend on the light field to be measured. Similarly we can calculate a sort of symmetry parameter

$$S_{x,\text{out}} = \frac{\sigma^{(3)}_{x,\text{out}}}{\overline{x}_{\text{out}}} = \frac{Q_{s,\text{det+dc}} - 3Q_{\text{det+dc}}}{\overline{m}^2_{\text{det+dc}}}\overline{x}^2_{\text{out}} + G\frac{1+3x_t}{1+x_t}\frac{Q_{\text{det+dc}}}{\overline{m}_{\text{det+dc}}}\overline{x}_{\text{out}} + G^2\frac{1+7x_t}{1+x_t} \, , \tag{18}$$

where $Q_{s,\text{det+dc}} = \sigma^{(3)}_{m,\text{det+dc}}/\overline{m}_{\text{det+dc}} - 1$. In the presence of dark counts both coefficients $(Q_{s,\text{det+dc}} - 3Q_{\text{det+dc}})/\overline{m}^2_{\text{det+dc}}$ and $Q_{\text{det+dc}}/\overline{m}_{\text{det+dc}}$ depend on the light being measured (Bondani et al., 2009a).

3.1.2 Method II: a numerical evaluation based on the photon-number resolving properties of SiPMs

The above mentioned self-consistent method is very powerful, but requires the acquisition of several histograms at varying η, which might not always be easily performed in practical applications: from this point of view, the possibility to analyze each spectrum independently looks complementary to the self-consistent approach. This analysis has been performed with a two-step procedure:

- the areas of the spectrum peaks have been computed in order to obtain an estimation of the number of counts per peak;
- the obtained data points have been fitted with a theoretical function, which takes into account the statistics of the light, the detection and all the deviations of the detectors from ideality, such as DCR and cross-talk effects.

To evaluate the area of each peak, we performed a multi-peak fit of the spectrum histogram modeling each peak with a Gauss-Hermite function (Van Der Marel et al., 1993):

$$\text{GH} = Ne^{-w^2/2}\left[1 + {}^3hH_3(w) + {}^4hH_4(w)\right] \tag{19}$$

where $w = (x - \bar{x})/\sigma$, N is a normalization factor, $\bar{x}$ the peak position and σ the variance of the Gaussian function. $H_3(w)$ and $H_4(w)$ are the third and the fourth normalized Hermite polynomials and their contribution gives the asymmetry of the peak shape, whose entity is regulated by the pre-factors ^3h and ^4h, with values in the range $[-1, 1]$. The global fit function of the spectrum is a sum of as many Gauss-Hermite functions as the number of resolved peaks.

By using Equation 19 it is possible to calculate the area A_n of the n-th peak as:

$$A_n = N_n \sigma_n (\sqrt{2\pi} + {^4h_n}). \tag{20}$$

The error σ_{A_n} has been calculated by propagating the errors on the fit parameters.
This analysis is also useful to estimate the system gain G: in fact, from the fitted values of the peak positions $\bar{x}_n$, the peak-to-peak distance Δ for all the resolved peaks is:

$$\Delta_{n,n+1} = \bar{x}_{n+1} - \bar{x}_n. \tag{21}$$

The associated error $\sigma_{\Delta_{n,n+1}}$ can be once again obtained by propagating the fit errors; furthermore, the value of G can be derived as a weighted average on all the peak-to-peak values obtained from the analysis of the histograms.

The effect of detection, DCR and amplification have been modeled as described in the previous Sections (see Equations 10-13 and Equation 16).

The effect of cross-talk has been described by using a Bernoullian process, in a way analogue to what has been done in Equation 14. However, as the cross-talk process is intrinsically a cascade phenomenon, its contribution has been calculated by adding higher order effects:

$$P_{k,cross} = \sum_{m=0}^{k} \sum_{n=0}^{m} \sum_{j=0}^{n} P_{k-m-n-j,det+dc} B_{m,k-m-n-j}(x_t) B_{n,m}(x_t) B_{j,n}(x_t); \tag{22}$$

where the terms like $B_{j,n}(x_t)$ stand for the Bernoullian distribution

$$B_{j,n}(x_t) = \binom{n}{j} x_t^j (1 - x_t)^{n-j}. \tag{23}$$

Such a higher order expansion is not trivial to be achieved by the self-consistent approach of *Method I*, in which an explicit analytic expression of $P_{x,out}$ is needed in order to calculate its moments. Here, as all the elements of interest ($\overline{m}_{el}$, $\overline{m}_{dc}$, x_t, the number of modes μ) will be obtained as parameters of a fit, this is not necessary and therefore $P_{x,out}$ can be just numerically computed as the fitting function.

The major limit of this approach is obvious: as all the information on the statistics of the system is obtained from the peak areas, this method can only be applied to peak-resolving histograms with a number of peaks larger than the number of free parameters of the fitting function, which, in the present analysis, can rise up to five.

3.2 Experimental results

In Ref. (Ramilli et al., 2010), we presented the experimental validation of the two complementary methods by using both coherent and pseudo-thermal light. In particular, we have demonstrated that it is not possible to use coherent light to derive the DCR contribution,
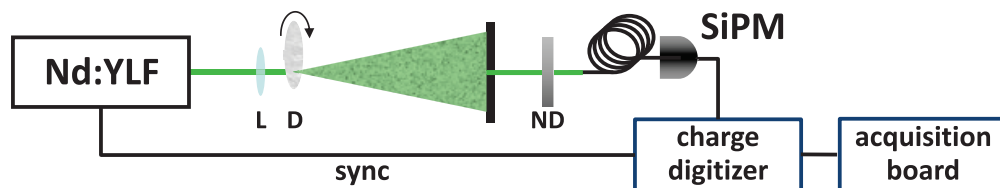
Fig. 9. Experimental setup. Nd:YLF: laser source, ND: variable neutral density filter, SiPM: detector.

which is described by a Poissonian distribution and is thus indistinguishable from the light under study. So we think that, within this context, it is more exhaustive and intriguing to show the results obtained with thermal light. The photon-number distribution of a field made of μ independent thermal modes is given by:

$$P_{n,\text{ph}} = \frac{(n+\mu-1)!}{n!\,(\mu-1)!\,(N_{th}/\mu+1)^{\mu}\,(\mu/N_{th}+1)^{n}} \,, \tag{24}$$

with $\overline{n} = N_{th}$, $\sigma_n^{(2)} = N_{th}\,(N_{th}/\mu+1)$ and $\sigma_n^{(3)} = N_{th}\,(N_{th}/\mu+1)\,(2N_{th}/\mu+1)$.

We reproduced a single mode of this pseudo-thermal light field by passing the coherent light of our laser source through an inhomogeneous diffusing medium and then selecting a single speckle with an aperture ($\sim 150\ \mu$m diameter), much smaller than the coherence area of the speckle pattern produced (Arecchi, 1965). By delivering this pseudo-thermal light to the SiPM sensor, we measured the values of the output, x, at 50000 subsequent laser shots and at 10 different mean values, obtained by means of a variable neutral-density filter (ND in Fig. 9). In Fig. 10 the plot of the experimental values of $F_{x,\text{out}}$ and $S_{x,\text{out}}$ is shown as a function of $\overline{x}_{\text{out}}$, along with the fitting curves evaluated from Equations 17 and 18:

$$F_{x,\text{out}} = \left(1 - \frac{\overline{x}_{\text{dc}}}{\overline{x}_{\text{out}}}\right)^2 \overline{x}_{\text{out}} + B$$

$$S_{x,\text{out}} = A\left(1 - \frac{\overline{x}_{\text{dc}}}{\overline{x}_{\text{out}}}\right)^3 \overline{x}_{\text{out}}^2 + 3B\left(1 - \frac{\overline{x}_{\text{dc}}}{\overline{x}_{\text{out}}}\right)^2 \overline{x}_{\text{out}} + C \,, \tag{25}$$

where μ, the number of independent thermal modes, has been set equal to one and, for simplicity of notation, the parameters $A = 2$, $B = G(1+3x_t)/(1+x_t)$ and $C = G^2(1+7x_t)/(1+x_t)$ have been introduced. We fitted the data to $F_{x,\text{out}}$ thus obtaining the values of $\overline{x}_{\text{dc}} = (5.82028 \pm 1.34015)$ and $B = (87.805 \pm 2.09009)$ ch.

Then the data for $S_{x,\text{out}}$ have been fitted substituting the above values of $\overline{x}_{\text{dc}}$ ch and B in order to obtain $A = (2.34754 \pm 0.091576)$ and $C = (8531.48 \pm 419.571)$ ch^2. These values were then used to evaluate G and x_t, obtaining $G = (74.2785 \pm 1.76982)$ ch and $x_t = (0.100174 \pm 0.050529)$. The x-values were then divided by G and re-binned in unitary bins (Bondani et al., 2009b) to obtain the $P_{k,\text{cross}}$ distribution of the actual light signal amplitude measured in the presence of dark counts and cross-talk. In Fig. 11 six different $P_{k,\text{cross}}$ distributions are plotted as bars at different mean values. Superimposed to the experimental values, two theoretical distributions are shown: the first one (white circles) is evaluated including the dark-count contribution that modifies the statistics of a single-mode thermal
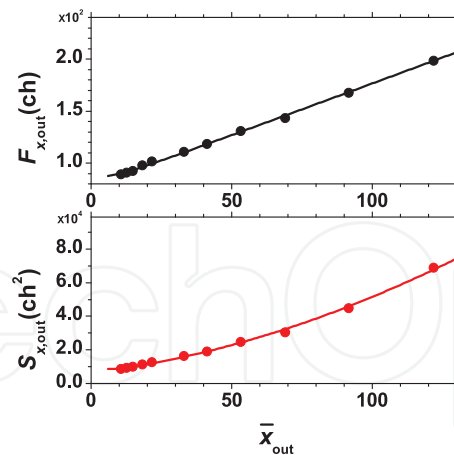
Fig. 10. Plot of $F_{x,\text{out}}$ and $S_{x,\text{out}}$ as functions of $\overline{x}_{\text{out}}$ for pseudo-thermal light.

distribution (see Equation 24) into

$$
\begin{aligned}
P_{m,\text{det}+\text{dc}} &= \sum_{k=0}^{m} P_{k,\text{dc}} P_{m-k,\text{det}} = \\
&= \frac{e^{-\overline{m}_{\text{dc}}}}{(\mu-1)!} \left(1 + \frac{\mu}{\overline{m}_{\text{det}}}\right)^{-m} \left(1 + \frac{\overline{m}_{\text{det}}}{\mu}\right)^{-\mu} \\
&\quad U\left[-m, 1-m-\mu, \overline{m}_{\text{dc}}\left(1 + \frac{\mu}{\overline{m}_{\text{det}}}\right)\right],
\end{aligned}
\tag{26}
$$

where $U(a, b, z)$ is the confluent hypergeometric function. The parameters are evaluated as $\overline{m}_{\text{dc}} = \overline{x}_{\text{dc}}/(G(1 + x_t))$ and $\overline{m}_{\text{det}} = (\overline{x}_{\text{out}} - \overline{x}_{\text{dc}})/(G(1 + x_t))$. The second curve (full circles) is evaluated from Equation 15 to take into account the cross-talk. Unfortunately, the calculation does not yield an easy analytical result, and hence it has been evaluated numerically.

The comparison between the data and the theoretical functions can be estimated through the evaluation of the fidelity $f = \sum_{k=0}^{m} \sqrt{P_{k,\text{exp}} P_{k,\text{theo}}}$ (see Fig. 11).

Turning now to the other approach, it is worth noting that the number of fit parameters is large: the probability distribution is described by the expectation value $\overline{m}_{\text{det}}$ of the avalanches generated by detection, the expectation value $\overline{m}_{\text{dc}}$ of DCR contribution, the number of modes μ, the probability x_t of triggering a cross-talk event (up to three "iterations") and again a global normalization factor, for a total of 5 fit parameters: obviously, this puts a severe limit on the applicability of this method, needing at least 6 resolved peaks.

As it can be noted from the fit results in Fig. 12, the results obtained by using *Method II* are compatible within errors with what we found by applying *Method I*. However, even if the global fits present a very low χ^2 value for degree of freedom, the obtained fit parameters present large uncertainties, probably indicating the presence of very large off-diagonal elements in the minimization matrix and suggesting a strong correlation between the various parameters. This problem can be avoided by fixing some of the fit parameters (such as DCR or cross-talk), once their values have been retrieved from an accurate direct measurement (see Section 2).
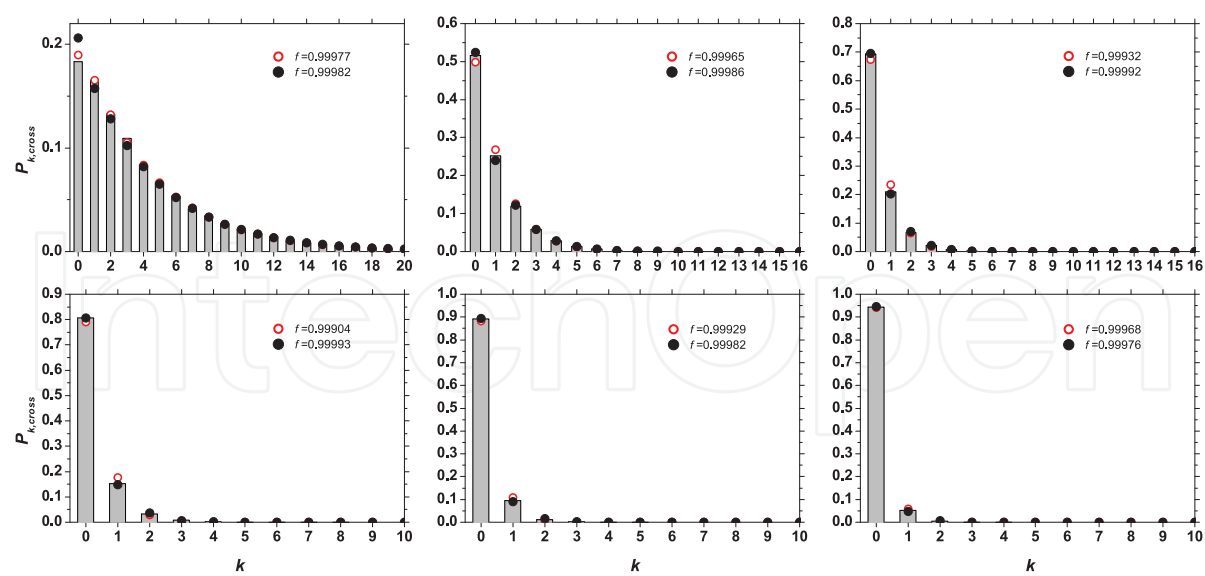
Fig. 11. Experimental $P_{k,\text{cross}}$ distributions at different mean values (bars) and theoretical distributions evaluated according to *Method I*: thermal modified by dark count distribution (white circles), thermal modified by dark counts and cross-talk effect (full circles). The corresponding fidelity values of the reconstruction are also shown.
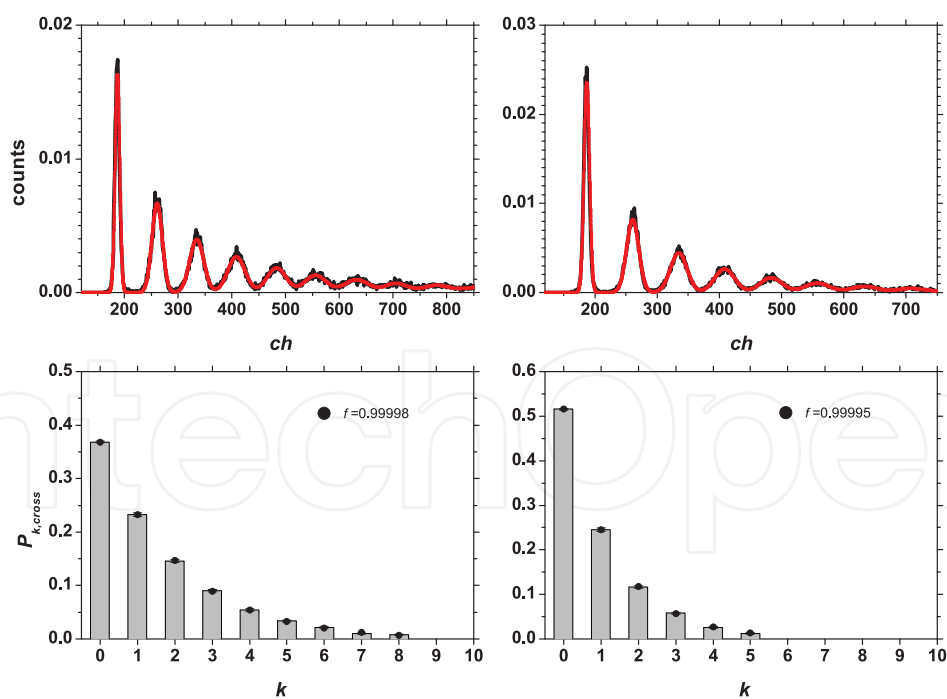

Fig. 12. Experimental results for *Method II* applied on two of the histograms acquired with thermal light. Upper panels: result of the multi-peak fit procedure; lower panels: fitted theoretical function. The corresponding fidelity values of the reconstruction are also shown.

3.3 Discussion

It is worth comparing the results of the two analysis methods on the same data sets (see Fig. 13). It is possible to notice that the agreement is better for the mean values of detected photons (panel (a)) and for the DCR (panel (b)), while the estimated values of x_t with the two *Methods* definitely disagree. This can be due to the different approximations adopted by the two *Methods* (first order *vs* third order).

In Table 3 we summarize the results of the two *Methods*. Both *Methods* work in a self-consistent way, even if they have two definitely different approaches. *Method I* does not need peak resolving capability, but requires the acquisition of several histograms at varying η. Once determined the parameters x_t and DCR, all the datasets in a series can be analyzed, independent of the number of distinguishable peaks in the pulse-height spectrum. *Method II* works analyzing each histogram independently, but, as the G-M-avalanches distribution is obtained with a fit of the data, it requires at least a number of resolved peaks larger than the number of free parameters.

The fact that the two *Methods* give very similar results for mean photon numbers is particularly important as in most applications this is the only important parameter. Merging the two *Methods* we can develop an optimal strategy based on a self-consistent calibration performed by measuring a known light and analyzing the data with *Method I*: once x_t and DCR are known, the determination of the mean photon number is independent of the specific light statistics. Hence the information on the mean photon number can be obtained from each single measurement, even when the fitting procedure of *Method II* cannot be applied.
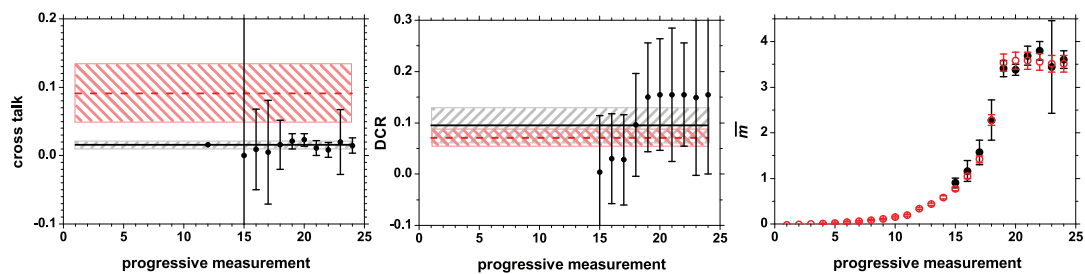

Fig. 13. Left panel: Cross- talk values of x_t obtained by applying *Method II* to thermal light (full circles) and their weighted average (full line). Dashed line: value of x_t obtained by *Method I*. Central panel: Values of DCR evaluated for the same data as in the left panel by applying *Method II* (full circles) and their weighted average (full line). Dashed line: value of DCR obtained by *Method I*. Right panel: Values of mean photon numbers evaluated by applying *Method II* (full circles) and by applying *Method I* (white circles).

	Pseudo-thermal	
	Method I	*Method II*
DCR	0.071 ± 0.017	0.094 ± 0.035
Cross-talk	0.091 ± 0.042	0.035 ± 0.004

Table 3. Comparison between the global DCR and cross-talk values obtained with *Method I* and weighted average of the values obtained with *Method II*.

4. Photon counting histogram with SiPM

Another instance in which the capability of resolving pulse-by-pulse the number of photons in high-repetition-rate periodic light signals is the analysis of fluorescence fluctuations. Traditionally, fluorescence techniques are applied to the study of systems constituted by huge ensembles of particles. For this reason, the probability distribution of the photon emission rate is peaked around its average value and fluctuations in the fluorescence signal are negligibly small. Nevertheless, if a microscopic system in which only few fluorophores are excited at a time is considered, the fluctuations in the fluorescence intensity become comparable to the average fluorescence intensity value, and can thus be measured. As these fluctuations are due to either the diffusion of the fluorophores in and out from the part of the specimen from which the fluorescence is collected and conveyed to the fluorescence detector, the so-called observation value, or to physical/chemical reactions inducing changes in the emission rate, their analysis can be applied both to characterize the diffusion kinetics and to study the physical/chemical reactions affecting emission. Such techniques are collectively called fluorescence fluctuation spectroscopy (FFS) techniques. This sort of analysis is particularly useful in probing biological systems both in vitro and in vivo. Indeed, many biomolecules (e.g. enzymes) and substances (such as minerals or ions) that are present in traces in cells have a determinant role in the cellular metabolism, and techniques allowing to study their action at physiological concentrations are most desirable. The most popular FFS technique is fluorescence correlation spectroscopy (FCS), which was developed in the early 1970′s (Gosch et al., 2005; Schwille, 2001), and consists in the analysis of the temporal correlations of fluorescence fluctuations in small molecular ensembles, combining maximum sensitivity with high statistical confidence. Among a multitude of physical parameters that are in principle accessible by FCS, it most conveniently allows to determine characteristic rate constants of fast reversible and slow irreversible reactions of fluorescently labelled biomolecules at very low (nanomolar and sub-nanomolar) concentrations. Moreover, the technique is a non-invasive one, which means that the above parameters can be assessed without perturbing the system equilibrium and, possibly, under physiological conditions. The technique also allows the determination of the mobility coefficients and local concentrations of fluorescent (or fluorescently labelled) molecules in their natural environments, provided that the exact value of the observation volume is known. More recently, at the end of the 1990′s, another FFS technique, called photon counting histogram (PCH), was developed by Chen et al. (Chen et al., 1999; 2005). This technique is based on the analysis of the statistical distribution of the fluctuations in amplitude of the fluorescence rate and is thus suited to yield steady state parameters of the system to be investigated, such as the number of different fluorescent species present in a solution, the average number of molecules of each species in the observation volume, and their molecular brightness, rather than dynamic parameters. This technique is thus to a certain extent complementary to FCS. Until now, both FCS and PCH measurements have been made by using APDs or other single-photon counters as the light detectors. Information on either the time-correlations or the statistical distribution of the fluorescence intensity fluctuations have been derived by counting the detection events in consecutive and equally long time intervals. As single-photon counters must be used only in the single photon regime (that is keeping the overall count rate very low in order to be sure that impingement on the detector sensitive area of photons during their dead time is a negligibly rare event), this sampling procedure is extremely time consuming and the sampling interval width must not be too small. Namely, in the most frequent case of pulsed excitation, it has to correspond to tens or even hundreds of pulse periods, which

means tens of microseconds or more. Obviously, this puts an inferior limit on the sensibility to fluorescence fluctuations occurring on time scales comparable, or shorter than, the sampling time. Conversely, many biological reactions occur on time scales of hundreds of nanoseconds to few microseconds (Nettels et al., 2007), that is slightly beyond the detection limit with the current procedures. We believe that the usage, for FFS techniques, of detectors able to count how many photons are contained in each fluorescence pulse could allow avoiding sampling. This will significantly and inherently enhance the temporal resolution of both techniques, virtually pulling it on the scale of the excitation source pulse period. Another advantage connected to the release of the single-photon regime operation condition is the possibility of performing statistically reliable measurements in much shorter times, which is notably beneficial for in-vivo analyses, as the samples quickly deteriorate. Recently, we have addressed the task of performing PCH analysis with SiPM detectors. Firstly, the standard PCH model developed for fitting data acquired with APDs (Chen et al., 1999; 2005) is not suitable to properly analyze the SiPM output; thus, the phenomenological model for describing the SiPM response presented above has been used to modify the PCH equations so as to take into account the deviations for ideal detection caused by the presence of optical cros-talk and sizeable DCR, leading to the following fitting model:

$$\Pi^\star\left(k; \bar{N}, \epsilon, x_t, \langle n \rangle_{dcr}\right) =$$

$$= \sum_{N=0}^{\infty} p_\#(N; \bar{N}) \sum_{m=0}^{k} C_{k,m}(x_t) \sum_{n=0}^{\infty} P_n(\langle n \rangle_{dcr}) p^{(N)}(m-n; \epsilon) \qquad (27)$$

where x_t is the parameter representing the probability for a cell of triggering a neighbour cell by cross-talk and $C_{k,m}(x_t)$ is the Bernoullian-like distribution defined in Section 3.1 describing the probability of measuring k G-M avalanches out of n previously triggered, with $k > m$. Secondly, a two-photon excitation setup has been commissioned and tested by performing standard PCH measurements on Rodamine B water solutions with a single-photon avalanche diode (PDM50, MPD) and a PC board allowing for real-time PCH reconstruction (SPC150, Becker & Hickl GmbH). The setup relied on fluorescence excitation by means of a continuous-wave SESAM mode-locked Ti:sapphire laser (Tiger-ps SHG, Time Bandwidth Product) delivering 3.9 ps pulses of 840 nm wavelength at a repetition rate of 48 Mhz. A 1.25 NA, 100X oil-immersion microscope objective (Nikon) was used both to focus the excitation beam onto the sample and to collect the emitted light in epifluorescence configuration. The fluorescence signal was separated from the back-scattered excitation light by using a dichroic mirror. Residual stray light was removed by using a short-wavelength-pass filter with cut at 700 nm. The fluorescence was delivered to the detector, through a 1 mm diameter multimode fiber. With this setup, appreciably superPoissonian PCH distributions were obtained for <300 nM dye solutions. Finally, a series of feasibility studies on the same dye were performed by using as the detector a Hamamatsu SiPM (MPPC S10362-11-100C). Given the 48 MHz repetition rate of the laser light source, the SiPM is expected to detect a fluorescence light pulse every 20 ns. In such experimental conditions, the usual detector signal processing seemed unfeasible with the instrumentation at hand by both the integration method and the free-time signal acquisition method. Indeed, in the first case the CAEN V792N QDC used for the quantum-light statistics measurements presented above requires an integration gate starting at least 15 ns before the rise of the signal, meaning that the board would not be able to process every pulse; moreover, with a detector recovery time of $\sim$ 60 ns, the output signal may exhibit pile-up features, which

in turn would lead to difficulties in reconstructing the photon statistics. In the second case, the DT5720A Desktop Digitizer at our disposal samples the output signal every 4 ns, which means that the signal integration would be performed using only 5 points. For these reasons, a completely different approach to process the detector signal was followed. Namely, the coincidence frequency $\nu(x)$ between a threshold scan of the SiPM output and a trigger signal ν_T synchronous with the laser pulses (but with a threefold reduced frequency) has been acquired. The measured frequency can be described by the following relation:

$$\nu(x) = \nu_T \left(1 - e^{-t_C \nu_S \int_x^{+\infty} \mathrm{d}y P(y)}\right) + \nu_T t_C \nu_S \int_x^{+\infty} \mathrm{d}y P(y); \tag{28}$$

where $P(y)$ is the probability of measuring a value y of the detector output signal, $\nu(x)$ is the threshold value, ν_S is the laser repetition rate and t_C is the coincidence time window. Equation 28 is based on the fact that a coincidence occurs both if after a trigger signal at least a SiPM signal over the threshold x is triggered within the coincidence time window or if the trigger signal rises within the coincidence time after the SiPM signal crosses the threshold. For small expectation values, Equation 28 can be approximated to

$$\nu(x) \approx 2\nu_T \nu_S t_C \int_x^{+\infty} \mathrm{d}y \, P(y). \tag{29}$$

Because of the Fundamental Theorem of Integration the detector output signal probability distribution can be written as

$$P(x) = \frac{-1}{2\nu_T \nu_S t_C} \frac{\mathrm{d}\nu(x)}{\mathrm{d}x} \tag{30}$$

which can be processed in the same way as the experimental detector output signal histograms experimentally obtained in the case of quantum-light statistics measurements to yield the probability distribution of the number of detected photons (see Section 3). In this set of measurements, the detector was controlled by the CAEN SP5600 General Purpose Power Supply and Amplification Unit module with an integrated threshold discriminator. The digital NIM output of the discriminator was put in coincidence with a synchronism signal triggered by the laser by using an EG&G CO4010 module. The coincidence frequency was sampled by a CAEN VME V1718. The fluorescence emission of two solutions of rhodamine B in water, with concentrations of 2 μM and 200 nM, respectively, have been analyzed with the threshold scan method described above. For the 2 μM concentrated solution a 1 optical density neutral filter was placed in front of the fiber, to reduce the mean detected fluorescence intensity to the value of the 200 nM concentrated solution. This makes the comparison between the two resulting distributions easier. Indeed, for equal expectation value, the 200 nM solution PCH should feature larger deviations from Poisson distribution, therefore showing a higher tail. Hereafter, the pertaining results are briefly summarized and their significance on the way towards implementation of PCH with SiPMs is outlined. Using Equation 30 the multi-peak spectra reported in Fig. 14 were obtained from the staircases for the 200 nM and the 2 μM solution, respectively. The PCH were derived from the spectra by applying the same procedure implemented in the quantum-light statistics data analysis. The zero-photons frequency was determined by imposing the normalization condition:

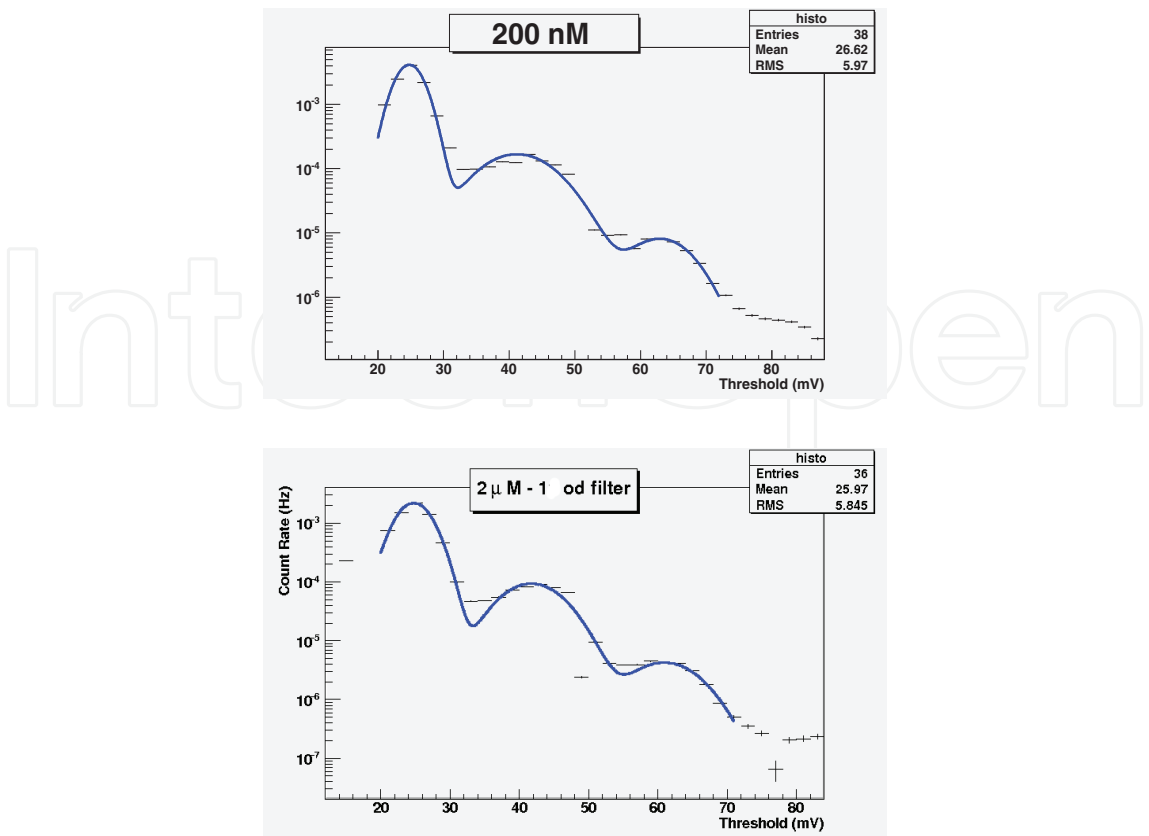$$\Pi^\star(0) = 1 - \sum_{k=1}^{L} \Pi^\star(k) \tag{31}$$

Fig. 14. Multipeak spectra of the fluorescence obtained from the threshold scans using Equation 30; in the upper panel spectrum from the 200 nM solution is shown, while in the lower panel the one obtained from the 2 μM solution is presented. Since the staircases has been acquired with a 2 mV step, histograms have 2 mV large bins. Spectra have been fitted with a multi-Gaussian function and the areas of each peak have been used as the PCH entries.

where L is the last detectable peak. The PCH are displayed in Figs. 15, for the 200 nM and the 2 μM solution, respectively. Fitting to Equation 27, with the average number of dark counts fixed to the experimental value preliminarily determined by performing a coincidence measurement of the dark counts, yields the fitting curves reported as dashed lines in Figs. 15.

The fitting parameters are summarized in Table 4.

Parameters	Concentrations (nM)	
	200	2000
$\bar{N}$	5.24 ± 0.03	71.70 ± 0.03
ϵ	$3.99 \times 10^{-3} \pm 2.4 \times 10^{-5}$	$1.536 \times 10^{-4} \pm 7 \times 10^{-7}$
x_t	$0.08085 \pm 5 \times 10^{-5}$	$0.0637 \pm 1 \times 10^{-4}$
$\langle n \rangle_{dcr}$	3.24×10^{-3}	3.24×10^{-3}

Table 4. Results for the fit of the PCH distributions. The errors listed are obtained from the fit procedure. The results for the mean number of particles and the molecular brightness are consistent with what expected, even though there is not exactly a factor 10 between the parameters of the two data sets.
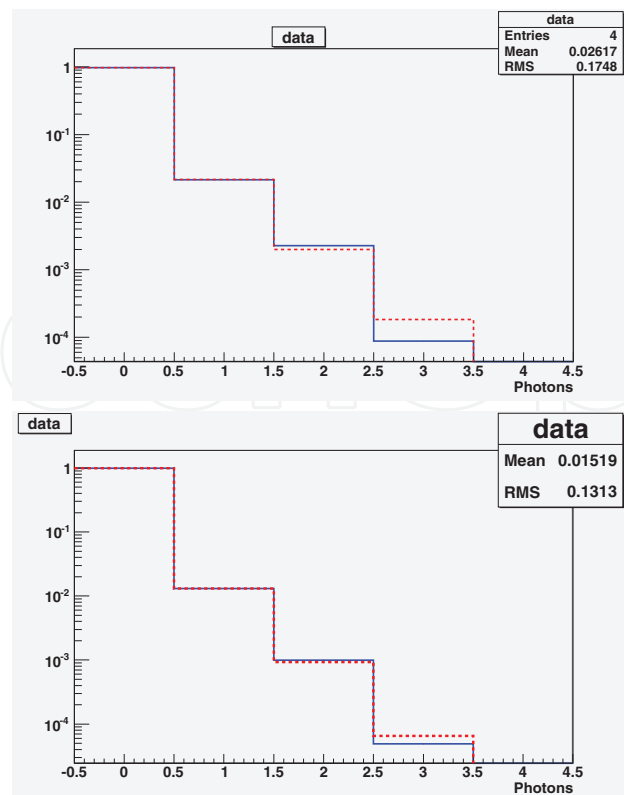
Fig. 15. Fit (red dashed line) of the experimental PCH data (blue continuous line) for 200 nM concentration (upper panel) and 2 μM concentration (lower panel).

The brightness and average particle number values are fairly consistent with the experimental conditions. Namely, the mean numbers of particles in the excitation volume differ by approximately one order of magnitude, reflecting the 10:1 concentration ratio between the two samples. To this purpose it should be noted that, while the concentration of the 2 μM solution could have been determined spectrophotometrically, 200 nM represents only a nominal value of the concentration of the less concentrated sample, obtained by dilution of the first, as the absorbance of it is below the sensitivity of our spectrophotometer ($\approx$ 0.001) in this case. Also the difference in molecular brightness is roughly consistent with the insertion of the 1-optical-density filter. Indeed, the fact that the molecular brightness measured for the 2 μM concentrated sample is found to be more than twenty times lower could be ascribed to a slight misalignment of either the laser or the microscope objective during the measurement session. The latter lasted for many hours due to the necessity of determining with high statistical reliability the very low frequencies of coincidences occurring at a high threshold value. Even a slight degeneration in the quality of the optical setup alignment would determine a notable decrease in the two-photon absorption cross section, which scales as the square power of the excitation intensity. This would be reflected in the brightness value. A broader focus is also consistent with the mean number of molecules in the excitation volume detected for the 2 μM solution, which is slightly larger than expected. Finally, the difference between the cross-talk values is consistent with a lower over-biasing condition for the 2 μM set, suggesting that a worsening of the photon detection efficiency could also have contributed to the lower molecular brightness. It must be admitted that the above presented procedure is very far from ideal pulse-by-pulse PCH acquisition. However, these preliminary data demonstrate that despite the relatively high dark count rates with respect to APDs

and the additional artifice constituted by optical cross-talk, SiPMs are detectors capable of discriminating the tiny deviations from Poisson distribution typically displayed by the PCH of diffusing fluorophores in solution at concentrations relevant for biophysical applications. Moreover, we notice that our fitting model yields consistent values of brightness and average fluorophore number. The above conclusions suggest that pulse-by-pulse reconstruction of PCH should be straightforwardly obtained with our detector and electronics apparatus for excitation rates <10 MHz, according to both the recovery time of the SiPM detector and the requirements of the CAEN integrator. An optical pulse-picker may be used to customize the Ti:sapphire repetition rate. Even working at such rates would allow to speed up PCH reconstruction by more than two orders of magnitude with respect to state-of-art APD-based methods. Alternatively, high-repetition rate measurements might be performed by reconstruction methods based on the analysis of the detector free-run output signal, as recorded by fast-sampling-rate digitizers. In such a case, the issues connected with detector pile-up effects would be overcome, thus confining the limits on the acquisition rate to the excitation rate and to the intrinsic decay time of the fluorophores under analysis.

5. Conclusions

We have presented the characterization of a class of photodetectors, namely the Silicon Photomultipliers, that has acquired great importance in the last decades because of its good photon-counting capability. Besides this feature, the compactness, robustness, low cost, low operating voltage and power consumption are added value that would make these detectors suitable for many applications. To this aim, we have implemented an exhaustive characterization protocol providing a quantitative evaluation of the main figures of merit these detectors are endowed with. In particular, we have studied the dependence of the photon detection efficiency, gain, dark count rate and optical cross-talk on temperature. The protocol has been applied to three SiPM detectors produced by different manufactures and the results have been then employed in a partnership with CAEN to develop the SP5600 General Purpose Power Supply and Amplification Unit module.

The versatility of SiPMs has been investigated in the reconstruction of the statistics of light states: two complementary models that take into account the DCR and the cross-talk effects have been developed in order to describe the output signal of the detectors. The correctness of these methods has been experimentally validated by illuminating the SiPM sensor with a single-mode pseudo-thermal light. However, further improvements could be achieved by including in the models the afterpulsing effect, which would become important in high-rate events.

The applicability of SiPMs in Fluorescence Fluctuation Spectroscopy studies has been preliminary evaluated by analyzing Rhodamine solutions by means of a Two-Photon Excitation setup: the capability of the sensors to reconstruct Photon Counting Histogram and in particular to provide the estimation of the mean number of fluorophores in the excitation volume and their molecular brightness has been proved.

6. References

Afek, I.; Natan, A.; Ambar, O.; & Silberberg, Y. (2009). Quantum state measurements using multipixel photon detectors. *Phys. Rev. A.*, Vol. 79, No. 4, April 2009, 043830, ISSN 1050-2947.

Agliati, A.; Bondani, M.; Andreoni, A.; De Cillis, G.; & Paris, M. G. A. (2005). Quantum and classical correlations of intense beams of light investigated via joint photodetection. *J. Opt. B Quantum Semiclass. Opt.*, Vol. 7, No. 12, November 2005, S652–S663, ISSN 1464-4266.

Akindinov, A. V.; Martemianov, A. N.; Polozov, P. A.; Golovin, V. M.; & Grigoriev, E. A. (1997). New results on MRS APDs. *Nuclear Instruments and Methods in Physics Research Section A: Accelerators, Spectrometers, Detectors and Associated Equipment*, Vol. 387, No. 1-2, March 1997, 231–234, ISSN 0168-9002.

Akindinov, A; Bondarenko, G.; Golovin, V.; Grigoriev, E.; Grishuk, Yu.; Malkevich, D.; Martemiyanov, A.; Ryabinin, M.; Smirnitskiy, A.; & Voloshin, K. (2005). Scintillation counter with MRS APD light readout. *Nuclear Instruments and Methods in Physics Research Section A: Accelerators, Spectrometers, Detectors and Associated Equipment*, Vol. 539, No. 1-2, February 2005, 172–176, ISSN 0168-9002.

Andreoni, A. & Bondani, M. (2009). Photon statistics in the macroscopic realm measured without photon counters. *Phys. Rev. A*, Vol. 80, No. 1, July 2009, 013819, ISSN 1050-2947.

Arecchi, F. T. (1965). Measurement of the Statistical Distribution of Gaussian and Laser Sources. *Phys. Rev. Lett.*, Vol. 15, No. 24, December 1965, 912–916, ISSN 0031-9007.

Bondani, M.; Allevi, A.; & Andreoni, A. (2009). Light Statistics by Non-Calibrated Linear Photodetectors. *Adv. Sci. Lett.*, Vol. 2, No. 4, December 2009, 463–468, ISSN 1936-6612.

Bondani, M.; Allevi, A.; Agliati, A.; & Andreoni, A. (2009). Self-consistent characterization of light statistics. *J. Mod. Opt.*, Vol. 56, No. 2, January 2009, 226–231, ISSN 0950-0340 print/ 1362-3044 online.

Chen, Y.; Müller, J. D.; So, P. T. C.; & Gratton, E. (1999). The Photon Counting Histogram in Fluorescence Fluctuation Spectroscopy. *Biophys. J.*, Vol. 77, No. 1, July 1999, 553–567, ISSN 0006-3495.

Chen, Y.; Tekmen, M.; Hillesheim, L.; Skinner, J.; Wu, B., & Muller, J. D. (2005). Dual-color photon counting histogram. *Biophys. J.*, Vol. 88, No. 3, March 2005, 2177–2192, ISSN 0006-3495.

Cova, S; Ghioni, M.; Lacaita, A.; Samori, C.; & Zappa, F. (1996). Avalanche photodiodes and quenching circuits for single-photon detection. *Appl. Opt.*, Vol. 35, No. 12, April 1996, 1956–1976, ISSN 1559-128X print/ 2155-3165 online.

Du Y. & Reti'ere, F. (2008). After-pulsing and cross-talk in multi-pixel photon counters. *Nuclear Instruments and Methods in Physics Research Section A: Accelerators, Spectrometers, Detectors and Associated Equipment*, Vol. 596, No. 3, November 2008, 396–401, ISSN 0168-9002.

Eckert, P.; Schultz-Coulon, H.-C.; Shen, W.; Stamen, R.; & Tadday, A. (2010). Characterisation studies of silicon photomultipliers. *Nuclear Instruments and Methods in Physics Research Section A: Accelerators, Spectrometers, Detectors and Associated Equipment*, Vol. 620, No. 2-3, August 2010, 217–226, ISSN 0168-9002.

Goetzberger, A.; McDonald, B.; Haitz, R. H.; & Scarlett, R. M. (1963). Avalanche Effects in Silicon p-n Junctions. II. Structurally Perfect Junctions. *Journal of Applied Physics*, Vol. 34, No. 6, June 1963, 1591–1600, ISSN 0021-8979.

Gösch, M. & Rigler, R. (2005). Fluorescence correlation spectroscopy of molecular motions and kinetics. *Adv. Drug. Del. Rev.*, Vol. 57, No. 1, January 2005, 169–190, ISSN 0169-409X.

Lutz, G. (1995). Silicon radiation detectors. *Nuclear Instruments and Methods in Physics Research Section A: Accelerators, Spectrometers, Detectors and Associated Equipment*, Vol. 367, No. 1-3, December 1995, 21–33, ISSN 0168-9002.

Mandel, L. & Wolf, E. (1995). *Optical Coherence and Quantum Optics*, Cambrige University Press, ISBN 0521417112, New York.

McKay, K. G. (1954). Avalanche Breakdown in Silicon. *Phys. Rev.*, Vol. 94, No. 4, May 1954, 877-884.

Nettels, D.; Gopich, I. V.; Hoffmann, A.; & Schuler, B. (2007). Ultrafast dynamics of protein collapse from single-molecule photon statistics. *Proc. Nat. Acad. Sci. USA*, Vol. 104, No. 8, February 2007, 2655–2660, ISSN 0027-8424.

Oldham, W. G.; Samuelson, R. R.; & Antognetti, P. (1972). Triggering phenomena in avalanche diodes. *IEEE Trans. Electron. Dev.*, Vol. 19, No. 9, September 1972, 1056-1060, ISSN 0018-9383.

Ramilli, M.; Allevi, A.; Chmill, V.; Bondani, M.; Caccia, M.; & Andreoni, A. (2010). Photon-number statistics with Silicon photomultipliers. *J. Opt. Soc. Am. B*, Vol. 27, No. 5, May 2010, 852–862, ISSN 0740-3224.

Schwille, P. (2001). Fluorescence correlation spectroscopy and its potential for intracellular applications. *Cell Biochem. Biophys.*, Vol. 34, No. 3, June 2001, 383–408, ISSN 1085-9195.

Sciacca, G.; Condorelli, E.; Aurite, S.; Lombardo, S.; Mazzillo, M.; Sanfilippo, D.; Fallica, G.; & Rimini, E. (2008). Crosstalk characterization in Geiger-mode avalanche photodiode arrays. *IEEE Electron. Dev. Lett.*, Vol. 29, No. 3, March 2008, 218-220, ISSN 0741-3106.

Tarolli, A.; Dalla Betta, G.-F.; Melchiorri, M.; Piazza, A.; Pancheri, L.; Piemonte, C.; & Zorzi, N. (2010). Characterization of FBK SiPMs under illumination with very fast light pulses. *Nuclear Instruments and Methods in Physics Research Section A: Accelerators, Spectrometers, Detectors and Associated Equipment*, Vol. 617, No. 1-3, May 2010, 430–431, ISSN 0168-9002.

Van Der Marel, R. P. & Franx, M. (1993). A new method for the identification of non-gaussian line profiles in elliptical galaxies. *Astrophysical Journal*, Vol. 407, No. 2, April 1993, 525–539, ISSN 0004-637X.

Zambra, G.; Bondani, M.; Spinelli, A. S.; Paleari, F.; & Andreoni, A. (2004). Counting photoelectrons in the response of a photomultiplier tube to single picosecond light pulses. *Rev. Sci. Instrum.*, Vol. 75, No. 8, August 2004, 2762–2765, ISSN 0034-6748 print/1089-7623 online.
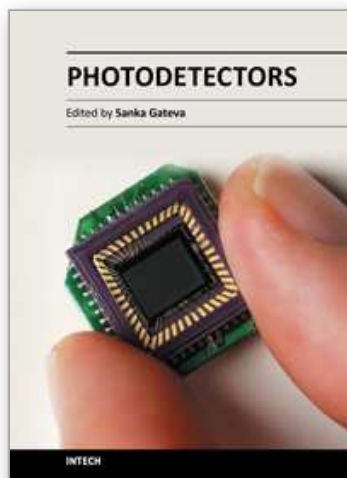
Photodetectors

Edited by Dr. Sanka Gateva

In this book some recent advances in development of photodetectors and photodetection systems for specific applications are included. In the first section of the book nine different types of photodetectors and their characteristics are presented. Next, some theoretical aspects and simulations are discussed. The last eight chapters are devoted to the development of photodetection systems for imaging, particle size analysis, transfers of time, measurement of vibrations, magnetic field, polarization of light, and particle energy. The book is addressed to students, engineers, and researchers working in the field of photonics and advanced technologies.

How to reference

In order to correctly reference this scholarly work, feel free to copy and paste the following:

INTECH
open science | open minds